Check for updates

Fabrication and thermal properties of novel myristic acid/MgO/BN composite phase change materials for thermal energy storage

Huan Zhang[1], Wenze Wang[1], Tingwei Fu[1], Guiyin Fang[1,a]

[1] School of Physics, Nanjing University, Nanjing 210093, China
a) Address all correspondence to this author. e-mail: gyfang@nju.edu.cn

A series of composite phase change materials (PCMs) were synthesized using myristic acid (MA) as the PCM, magnesium oxide (MgO) and hexagonal boron nitride (h-BN) as both support materials and thermal conductivity enhancers. Leakage experiments indicate that the total mass fraction of MgO and h-BN reaches about 20 wt% to eliminate the leakage. FT-IR and XRD results confirm that MA, MgO and h-BN are physically combined with each other. SEM images show that MA is filled into the voids of MgO and h-BN. DSC analysis indicates that the composites have two melting processes. Thermogravimetric results show that the composites have excellent thermal stability at the melting temperature. Thermal conductivity results show that the thermal conductivity of composites can be improved by incorporating h-BN at the same MgO content. In addition, the thermal conductivity can be significantly improved by introducing h-BN compared to adding MgO.

Introduction

The energy crisis is a commonly discussed topic, and the direction to solve such problems is the development of renewable new energy, such as solar energy, geothermal energy, wind energy, etc.; the other direction is the exploration of new energy storage media, which can effectively solve the problem of uneven distribution of energy, and can greatly improve the efficiency of energy utilization [1]. Recently, thermal energy storage technology has received more attention due to the fact that thermal energy is the most abundant type of energy in nature. Generally, there are sensible thermal energy storage, latent thermal energy storage and thermochemical energy storage. Among the three thermal energy storage, latent thermal energy storage is highly regarded for its high energy storage density and wide temperature range [2]. This technology uses the change of physical state of the working material to achieve heat storage and release, so it can be divided into four ways: solid–solid, solid–liquid, solid–gas and liquid–gas [3]. The latter two are not suitable for practical applications because of the large volume changes that would take place, so only the first two have attracted interest. In particular, solid–liquid phase change materials (PCMs) are widely used in buildings [4, 5], thermal management [6] and heat recovery systems [7].

There are two main categories of solid–liquid PCMs, namely organic PCMs and inorganic PCMs [8]. Compared with inorganic PCMs, organic PCMs have the merits of low supercooling, no phase separation, good chemical stability, and non-corrosiveness, so they are widely used in current research, such as paraffin [9], fatty acids [10] and alcohols [11]. Since fatty acid PCM possess high phase change enthalpy, self-nucleation [12], non-toxicity, and low cost [13], they are proposed to be potential PCM. Nevertheless, solid–liquid organic PCMs have unavoidable defects, one is the tendency to leak in the molten state and the other is the low heat transfer rate, and these defects greatly suppress their applications. To overcome these drawbacks, combining support material with PCM to form shape-stabilized PCM is an effective strategy [14].

In general, the choice of matrix material directly affects the thermal properties of the PCM. High-density polyethylene (HDPE), polystyrene (PS), SiO_2, diatomite, expanded perlite (EP), etc. have been widely considered as matrix materials [15–17]. For example, Rahman et al. [18] fabricated paraffin/HDPE shape-stabilized PCM. Ke et al. [19] synthesized a polystyrene-based shape-stabilized PCM with a phase transition temperature tunable to a lower temperature range. Baskar

et al. [20] synthesized a composite PCM using eutectic lauric and palmitic acids as the PCM and nano-SiO_2 as the support material. The melting enthalpy of the composites reaches 187 J/g, and the thermal conductivity value is increased by 54.4%. Benayache et al. [21] prepared a paraffin/diatomite shape-stabilized PCM by impregnating paraffin into diatomite. This composite exhibits excellent thermal reliability and thermal storage performance. Although the polymer matrix and the clay mineral matrix are able to eliminate leakage well, the thermal conductivity of the composite is not significantly improved.

In contrast, nanometal oxides [22, 23] and hexagonal boron nitride (h-BN) [24, 25] have not only excellent thermal stability but also excellent thermal conductivity, so their addition can both prevent melt leakage and significantly improve the thermal conductivity of PCM. Samiyammal et al. [26] reported that the thermal conductivity of paraffin-based composites is enhanced by the incorporation of magnesium oxide nanoparticles. Xie et al. [27] fabricated composite PCM by stripping h-BN from the native material and using it as a support material. The melting enthalpy of the composite PCM is 136.2 J/g and thermal conductivity is improved to 0.453 W/(m·K). Fang et al. [28] synthesized composite PCM composed of paraffin and h-BN. The results indicate that 10 wt% of h-BN is able to improve the thermal conductivity of composites by 60%. Accordingly, MgO and BN can be served as support materials and also as thermal conductivity enhancers for PCM.

The purpose of this work is to prepare a shape-stabilized PCM that has no significant decrease in latent heat and a significant improvement in thermal stability and thermal conductivity. MA was adopted as a PCM because of its advantages such as high latent heat and its availability for solar water heating systems. Combinations of nano-MgO and h-BN were acted as both matrix materials and thermal conductivity enhancers. Shape-stabilized PCMs were prepared by the melt blending method. The composite PCMs were tested for leakage and their structural characteristics and surface morphology were analyzed. Thermophysical properties of composite PCMs were also determined to evaluate their potential for thermal storage applications.

Results and discussion

Leakage testing analysis

The leakage of the samples can be evaluated by subjecting them to a leakage test. The specific experimental scheme is as follows: place the sample on a clean white paper and place it on the heater with the temperature maintained at 65 °C. After 15 min, the sample is removed. The area of oil stains on the white paper reflects the degree of leakage of the sample. Figure 1 shows nine samples and their leakage test results. It is clear that when the level of h-BN is certain, the area of the oil stain is gradually reduced with the addition of MgO content. When the MgO content is certain, the area of the oil stains gradually decreases with increasing h-BN content. These results indicate that the addition of MgO and h-BN can effectively prevent the leakage of molten MA, and both serve as support materials. In addition, the C6-C9 samples have almost no leakage, so they will be further tested and analyzed.
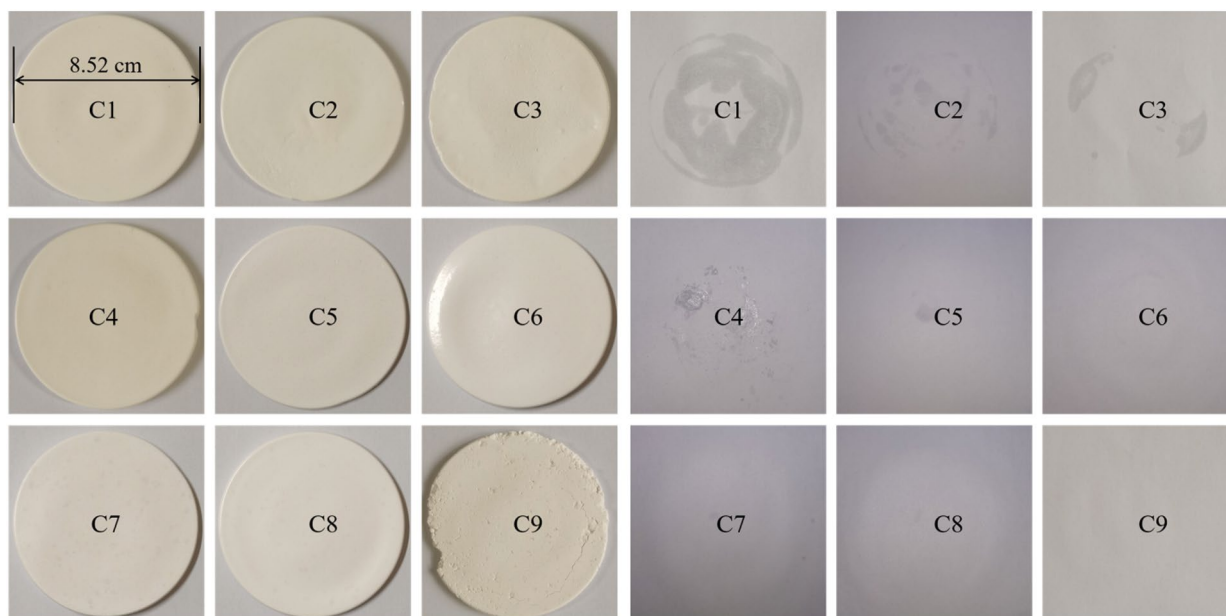

Figure 1: MA/MgO/h-BN composite PCMs and their leakage test results.

FT-IR analysis

The FT-IR spectra of MA, MgO, h-BN and C6-C9 are shown in Fig. 2(a). Four representative peaks at 2917, 2850, 1700, and 721 cm^{-1} can be observed in the spectrum of MA. Among them, the peaks at 2917 and 2850 cm^{-1} indicate the anti-symmetric and symmetric stretching vibrations of the -CH$_2$ group; the peak at 1700 cm^{-1} represents the stretching vibrations of the C=O group; and the peak at 721 cm^{-1} reflects the presence of four or more –CH$_2$ groups in the molecular chain [29]. The spectrum of MgO shows that it does not have a more pronounced characteristic absorption peak at 3500–700 cm^{-1}. The pattern of h-BN shows the characteristic peaks at 1391 and 807 cm^{-1}, which are the bending and stretching vibrations of the B-N bond [27]. The C6-C9 spectra indicate that their absorption peak positions correspond to those of MA and h-BN one by one, and no new characteristic peaks appear, confirming that no chemical reaction occurs during the preparation of the composites. Therefore, the combination of MA, MgO and h-BN is only a physical interaction.

XRD analysis

The XRD spectra of MA, MgO, h-BN and C6-C9 are shown in Fig. 2(b), reflecting the corresponding crystal structures. It can be seen that the diffraction curve of MA has a sharp strong peak at 21.6°, a secondary strong peak at 24.4° and a weak peak at 20.3°, which reflects the regular crystallization of MA [29]. The diffraction peak of MgO is located at 42.8°. The h-BN shows a sharp characteristic peak at 26.6°, which is attributed to the typical (0 0 2) crystal face [27]. As observed from the diffraction curves of C6-C9, the position of the characteristic peak of MA remains basically the same and its intensity is significantly

weakened, but the peak at 24.1° evolves into a dispersion peak. In addition, the characteristic peaks of MgO and h-BN are also present in C6-C9, and only the peak intensity has been decreased. Furthermore, there are no diffraction peaks other than MA, h-BN and MgO, indicating that the XRD spectra of C6-C9 are essentially composed of the spectra of MA, MgO and h-BN. Therefore, the mixing of MA, MgO and h-BN does not yield new materials.

Microstructure analysis

The microscopic morphologies of MA, MgO, h-BN and C6-C9 are presented in Fig. 3. As observed in Fig. 3(a), MgO appears as smaller particles with more voids. In Fig. 3(b), h-BN is a two-dimensional lamellar structure. Figure 3(c)–(f) correspond to the microstructures of C6-C9. MgO and h-BN show a more uniform dispersion and MA is adsorbed in the voids. Due to the surface tension and capillary force, the bond between MA, MgO and h-BN is stable and can effectively restrict the leakage of liquid phase MA.

Thermal performance analysis

The DSC curves of MA and C6-C9 are shown in Fig. 4, where Fig. 4(a) shows the melting process and Fig. 4(b) shows the solidification process. The relevant measurements obtained from these samples are shown in Table 1 in terms of melting/solidification temperature (T_m/T_s), peak temperature (T_{pm}/T_{ps}), and latent heat of melting/solidification ($\Delta H_m/\Delta H_s$). In Fig. 4(a), pure MA has only one sharp heat absorption peak, which denotes the solid–liquid transition of MA with a latent heat and melting point of 197.50 J/g and 54.83 °C, respectively. However, the melting process of C6-C9 is significantly different
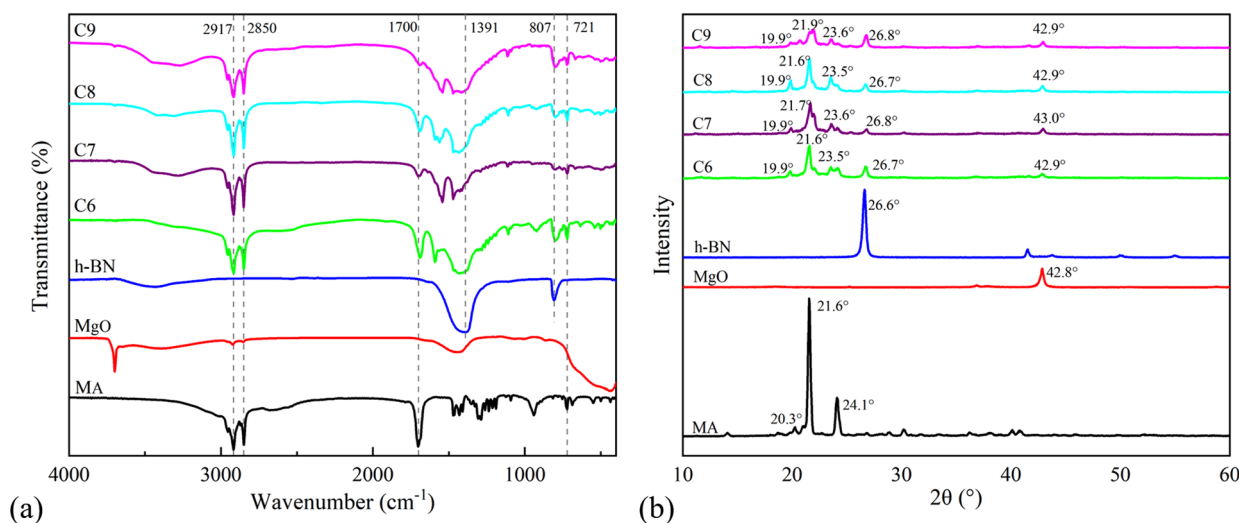

Figure 2: The spectra of MA, MgO, h-BN and C6-C9. (a) FT-IR spectra. (b) XRD spectra.
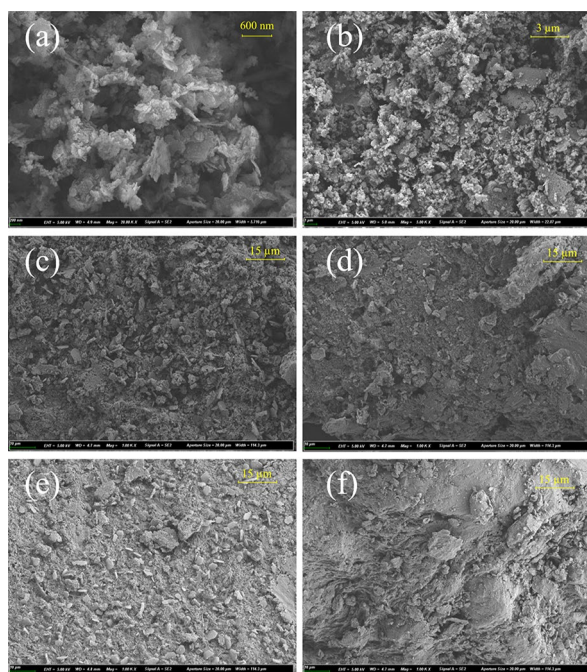
Figure 3: SEM images. (a) MgO. (b) h-BN. (c)–(f) C6-C9.

from that of pure MA in that they have two heat absorption peaks. The melting points of the first heat absorption peaks of C6-C9 are 51.34, 51.90, 51.23 and 51.14 °C, respectively, which are about 3 °C lower than the melting point of pure MA. The first heat absorption peaks are similar to the absorption peak of pure

MA, but they are significantly smaller and the shoulders become slightly broader. The melting points of the second heat absorption peaks of C6-C9 are 70.58, 70.22, 70.87 and 66.77 °C, respectively, which are about 16 °C higher than the melting point of pure MA. The second heat absorption peaks are smoother and their shoulders are much broader. In Fig. 4(b), pure MA also has only one sharp exothermic peak with a latent heat and solidification point of 197.30 J/g and 51.93 °C, respectively. The exothermic peaks of C6-C9 are similar to the exothermic peak of pure MA, but their peaks are obviously smaller and their shoulders become broader. The solidification temperatures of C6-C9 are 40.34, 39.86, 41.01 and 43.60 °C, respectively, which are about 10 °C lower than the solidification temperature of pure MA.

Composite PCMs exhibit two heat absorption peaks during melting, which are also observed in the works of Li [30] and Yang [31]. In this study, the first heat absorption peak of the composite PCMs is consistent with the usual situation, while the temperature of the second heat absorption peak is significantly elevated. The appearance of this anomalous heat absorption peak can be regarded as a result of superimposed forces based on the Young–Laplace equation. These forces include C-H…π interactions [32], surface tension [30], hydrogen bonding, and van der Waals forces [33]. For composite PCMs, there are large interactions and pressure superposition between the MgO matrix and the confined MA, and this superimposed pressure in the confined space leads to an elevation of the phase transition temperature.
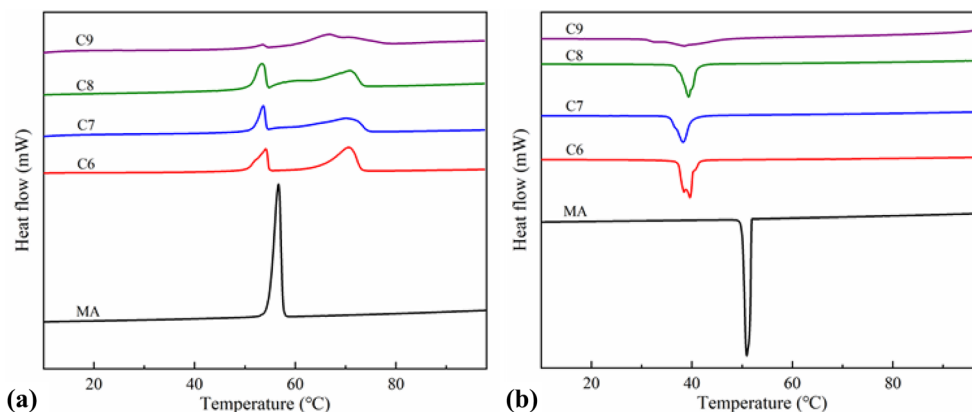

Figure 4: DSC curves of MA and C6-C9. (a) Melting process. (b) Solidification process.

TABLE 1: DSC results of MA and C6-C9.

Samples	T_m (°C)	T_{pm} (°C)	ΔH_m (J/g)	T_s (°C)	T_{ps} (°C)	ΔH_s (J/g)
MA	54.83	56.66	197.50	51.93	50.96	197.30
C6	51.34/65.01	54.10/70.58	42.63/97.82	40.34	39.58	100.61
C7	51.90/60.54	53.66/70.22	25.71/82.17	39.86	38.22	79.28
C8	51.23/60.12	53.38/70.87	40.79/110.62	41.01	39.38	79.77
C9	51.14/59.14	53.56/66.77	2.32/44.13	43.60	38.61	36.27

The total melting latent heats of C6-C9 are 140.45, 107.88, 151.41 and 46.45 J/g, respectively. Dividing the total melting latent heat by that of pure MA, the mass fractions of MA in composite PCM are 71%, 55%, 77% and 24%, respectively. As for the formulation of MA/MgO/h-BN, the mass fractions of MA are 78%, 82%, 78% and 74%, respectively. It is clear that the latent heat drop in C9 is large, and this reduction may be caused by the presence of non-melting layers in the composite [34]. Therefore, among the obtained composites, C6 and C8 have more satisfactory high latent heat of phase change.

Thermal stability analysis

Figure 5(a) and (b) show the TGA and DTG curves of MA, MgO, h-BN and C6-C9, respectively, which can reflect the thermal stability of these samples. Table 2 presents the key data of the thermal decomposition process with the peak temperature (T_p) and the specific weight of mass loss (ΔW), as well as the mass residue at 700 °C. It can be seen that MA has an obvious one-step weight loss process in Fig. 5(a), which is more stable below 150 °C. The thermal decomposition rate reaches the maximum at 234.61 °C, and the mass residue is only about 3.5%. MgO shows a very slightly weight loss at 30–300 °C, which can be considered as a moisture-induced loss. There is a significant weight loss at 300–400 °C, and the thermal decomposition rate reaches the maximum at 361.74 °C, with a final weight loss ratio of about 17.4%. The h-BN is very stable, and it almost does not undergo thermal degradation. Unlike the pure MA, the MA/MgO/h-BN composites all show a distinct two-step weight loss process, with two distinct peaks in the Fig. 5(b). The first step is between about 150–250 °C, which can be considered as the lesser MA decomposition process, and the maximum pyrolysis rate of this process is significantly lower than that of pure MA. The weight loss percentage of C6 is about 31%, while that

TABLE 2: Thermogravimetric data of MA, MgO and C6-C9.

Samples	T_{p1} (°C)	ΔW_1 (%)	T_{p2} (°C)	ΔW_2 (%)	Residue (%)
MA	234.61	96.51	–	–	3.49
MgO	–	–	361.74	17.43	82.57
C6	199.74	31.29	386.39	47.26	21.45
C7	194.39	12.70	388.75	70.15	17.15
C8	185.04	16.57	387.59	61.84	21.59
C9	199.51	7.79	379.17	66.99	25.22

of C7-C9 is much lower. The second step is about 300–500 °C. This process involves decomposition of a small amount of MgO and the remaining MA, and the weight loss ratio of C6 is about 47%, while C7-C9 is over 60%. The final pyrolysis mass residue belongs to MgO and h-BN. Compared with the MgO decomposition curve in Fig. 5(a), the second weight loss process of the composites corresponds to the weight loss process of MgO, indicating that the decomposition process is mainly caused by the strong limiting effect of MgO. Overall, the pyrolysis process of the samples confirms that the composites are almost stable below 150 °C, while the two-step thermal decomposition process can be attributed to the strong limiting effect of MgO, which leads to the secondary weight loss of the composites.

Thermal conductivity analysis

To evaluate the heat transfer efficiency of the composite PCMs, the thermal conductivity of the nine samples is measured. The thermal conductivity of pure MA is only 0.20 ± 0.01 W/(m·K), while the thermal conductivity of composite PCMs is increased by the addition of the support material. The thermal conductivities of C1-C9 composites are 0.29 ± 0.02, 0.37 ± 0.01, 0.47 ± 0.02, 0.32 ± 0.01, 0.41 ± 0.02, 0.52 ± 0.02, 0.37 ± 0.01, 0.44 ± 0.02 and

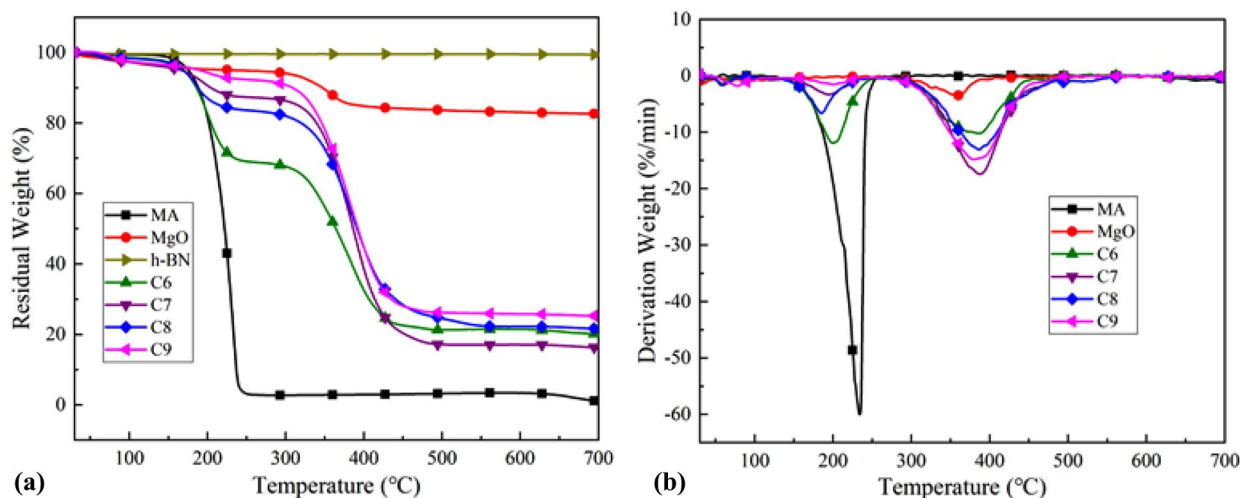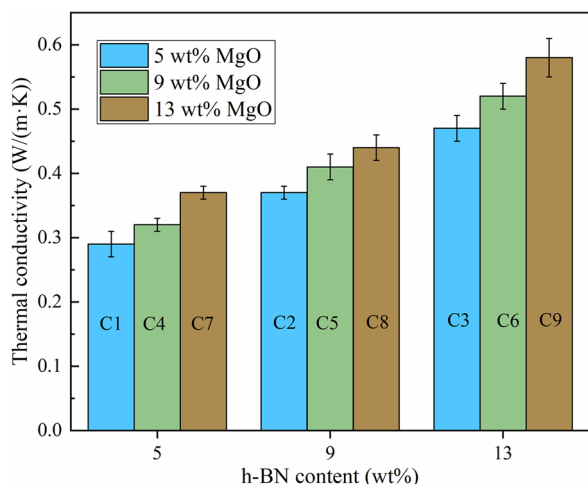**Figure 5:** Thermogravimetric curves of MA, MgO, h-BN and C6-C9. (a) TGA curve. (b) DTG curve.

Figure 6: Thermal conductivity of C1–C9.

not only have high latent heat but also have good thermal conductivity. Therefore, the composite PCMs prepared in this work have potential applications.

Conclusions

In this paper, a series of MA/MgO/h-BN composite PCMs were prepared by the melt blending method using MA as the PCM and combinations of nano-MgO and h-BN as the support material and thermal conductivity enhancer. Leakage test results show that molten MA leakage is eliminated when the total mass ratio of MgO and h-BN is about 20 wt%, and the higher the MgO content, the less leakage occurs. FT-IR and XRD results indicate that the components of composite PCMs are combined with each other in a physical interaction. SEM results suggest that MA is filled into the voids of MgO and h-BN. Thermal analysis shows two heat absorption peaks for the melting process of C6–C9, which is attributed to the presence of a large superposition pressure between the confined MA and the MgO/BN matrix, leading to a significant increase in the phase transition temperature. Thermogravimetric experiments indicate that the composite PCMs are almost stable below 150 °C. The second weight loss process reflects the limiting effect of the MgO matrix on MA due to the fact that large amounts of MA in the composite PCMs are pyrolyzed in the second weight loss process, whereas originally all MA should have been pyrolyzed in the first weight loss process. Thermal conductivity measurements show that the thermal conductivity of the composite PCM improves with increasing h-BN when the mass fraction of MgO is fixed. Although both MgO and h-BN have the effect of improving the thermal conductivity, the thermal conductivity improved by adding h-BN is significantly better than that of MgO. Therefore, in the prepared MA/MgO/h-BN composite PCMs, both MgO and h-BN are available as matrix materials and thermal conductivity enhancers, but their effects are quite different. MgO mainly affects the phase transition temperature and latent heat of the composite PCMs, while h-BN mainly affects the thermal conductivity of the composite PCMs. In summary, C6 has good thermal properties. Its melting latent heat is 140.45 J/g and its thermal conductivity is 0.52 W/(m·K). The thermal conductivity of C8 is 0.44 W/(m·K), which is slightly lower than that of C6. However, its melting latent heat is higher than that of C6, which is 151.41 J/g.

0.58 ± 0.03 W/(m·K). Compared with pure MA, the thermal conductivity is increased by 45%, 85%, 135%, 60%, 105%, 160%, 85%, 110% and 190%, respectively. In particular, the increase in thermal conductivity of C6–C9 is more than 85%. For a more visual comparison, the thermal conductivity data are plotted as histograms in Fig. 6. As can be seen, the thermal conductivity of composite PCMs is only slightly increased with the increase of MgO when the h-BN mass fraction is a certain amount. When the mass fraction of MgO is fixed, there is a large increase in the thermal conductivity of composite PCMs with increasing h-BN. In other words, h-BN can be more effective than MgO in the improvement of the thermal conductivity of composite PCMs.

In Table 3, the current study is compared with other literature [34–38]. The composite PCMs obtained in this experiment

Experimental methods

Materials

Myristic acid (MA, $C_{14}H_{28}O_2$, molecular weight: 228.37, content ≥ 98.0%, chemically pure) was sourced from Sinopharm Chemical Reagent Co., Ltd. It shows a white blade-like

TABLE 3: Comparison of the thermal conductivity between this work and other results.

Samples	Latent heat (J/g)	Thermal conductivity (W/(m·K))	References
n-Eicosane (60%)/EP	161.18	0.15	[8]
Stearic acid (70%)/ HDPE	135.46	0.35	[35]
Palmitic acid (30%)/ mullite	52.30	0.52	[36]
Capric acid (17.5%)/ kaolin	27.23	0.23	[37]
n-Octadecane (60%)/ PS	72.38	0.15	[38]
Stearic acid (80%)/ Al₂O₃	196.73	0.50	[39]
Erythritol (70%)/Vermiculite	216.70	0.40	[40]
MA/MgO/h-BN (C6)	140.45	0.51	This work
MA/MgO/h-BN (C8)	151.41	0.44	This work

TABLE 4: Constitution of MA/MgO/BN composites.

Samples	MA (g)	MgO (g)	BN (g)	Mass fraction of MA (%)
C1	27.0	1.5	1.5	90
C2	25.8	1.5	2.7	86
C3	24.6	1.5	3.9	82
C4	25.8	2.7	1.5	86
C5	24.6	2.7	2.7	82
C6	23.4	2.7	3.9	78
C7	24.6	3.9	1.5	82
C8	23.4	3.9	2.7	78
C9	22.2	3.9	3.9	74

crystalline powder with a melting point of approximately 52.5 to 54.5 °C. Magnesium oxide nanoparticles (MgO, purity: 98%, specific surface area (SSA): 42.05 m^2/g) and high-purity hexagonal nitride boron (h-BN, purity $\geq$ 99.5%) nanoplates were provided from Jiangsu XFNANO Materials Tech Co., Ltd. MgO is a white powder with a particle size of about 20 nm. h-BN is also a white powder with a sheet length of about 0.3–2 μm.

Preparation of MA/MgO/h-BN composites

In this work, MA/MgO/h-BN composite PCMs were prepared by melt blending technique. The weights of the components in these composites are listed in Table 4. The detailed preparation procedures for the MA/MgO/h-BN composite PCM are as follows: first, each substance is weighed according to the masses assigned in Table 4 and put into a beaker. Then, the beaker containing MA is placed on a heater and the temperature is maintained at 60 °C so that the MA is completely melted; when the MA is completely melted, the corresponding h-BN is added and stirred at 1000 rpm for 10 min by a cantilevered mechanical stirrer; next, the corresponding MgO is gradually added and stirred at 1000 rpm for 1 h to ensure uniform dispersion. Finally, the molten composite is poured into a glass dish and allowed to cool naturally. The above preparation process is repeated to obtain nine products, which are labeled in sequence as C1, C2, C3, C4, C5, C6, C7, C8 and C9, as shown in Fig. 1.

Instruments and characterization techniques

Structural characterization

Fourier transform infrared (FTIR, Nicolet Nexus 870) spectroscopy is adopted to measure the chemical groups of the composites. Wavenumbers range from 4000 to 400 cm^{-1} with 2 cm^{-1}

resolution. X-ray diffraction (XRD, D/MAX-Ultima III) is employed to characterize the crystal structure of the composites. The working parameters of XRD are: scanning speed 5° (2θ)/min, voltage 40 kV, and current 40 mA. Ultra-high resolution scanning electron microscope (SEM, Gemini 500, Carl Zeiss, Germany) is utilized to observe the microscopic morphology of composites.

Thermal behavior characterization

Differential scanning calorimetry (DSC) is used to determine the relevant parameters (phase change point and phase change enthalpy) of composite PCM in the phase change process with an accuracy of $\pm$ 0.2 °C for temperature and $\pm$ 5% for enthalpy. The operating temperature and heating/cooling rate of the DSC are set to 10–100 °C and 5 °C /min, respectively. A thermogravimetric analyzer (TGA, Perkin-Elmer Pyris 1) is implemented to evaluate the thermal stability of the composites. The working temperature and heating rate of the TGA were configured to 30–700 °C and 20 °C/min, respectively. The TC3020 transient hot-wire conductivity meter is employed to measure the thermal conductivity of the composites with an accuracy of $\pm$ 2%.

Data availability

Data will made available on reasonable request.

Declarations

Conflict of interest On behalf of all authors, the corresponding author states that there is no conflict of interest.

References

1. S.K. Mangla, S. Luthra, S. Jakhar, S. Gandhi, K. Muduli, A. Kumar, A step to clean energy-sustainability in energy system management in an emerging economy context. J. Clean. Prod. **242**, 118462 (2020)

2. X. Zhu, L. Han, F. Yang, J. Jiang, X.L. Jia, Lightweight mesoporous carbon fibers with interconnected graphitic walls for supports of form-stable phase change materials with enhanced thermal conductivity. Sol. Energy Mater. Sol. Cells **208**, 110361 (2020)

3. H. Zhang, C.L. Xu, G.Y. Fang, Encapsulation of inorganic phase change thermal storage materials and its effect on thermophysical properties: a review. Sol. Energy Mater. Sol. Cells **241**, 111747 (2022)

4. S. Mousavi, B. Rismanchi, S. Brey, L. Aye, PCM embedded radiant chilled ceiling: a state-of-the-art review. Renew. Sustain. Energy Rev. **151**, 111601 (2021)

5. I. Baskar, M. Chellapandian, S.S.H. Jaswanth, Development of a novel composite phase change material based paints and mortar for energy storage applications in buildings. J. Energy Storage **55**, 105829 (2022)

6. Q.L. Ren, P.H. Guo, J.J. Zhu, Thermal management of electronic devices using pin-fin based cascade microencapsulated PCM/expanded graphite composite. Int. J. Heat Mass Transf. **149**, 119199 (2020)

7. A.A.M. Omara, Phase change materials for waste heat recovery in internal combustion engines: a review. J. Energy Storage **44**, 103421 (2021)

8. A. Karaipekli, A. Biçer, A. Sari, V.V. Tyagi, Thermal characteristics of expanded perlite/paraffin composite phase change material with enhanced thermal conductivity using carbon nanotubes. Energy Convers. Manage. **134**, 373–381 (2017)

9. Z.J. Chang, K. Wang, X.H. Wu, G. Lei, Q.W. Wang, H. Liu, Y.L. Wang, Q. Zhang, Review on the preparation and performance of paraffin-based phase change microcapsules for heat storage. J. Energy Storage **46**, 103840 (2022)

10. A. Al-Ahmed, M.A.J. Mazumder, B. Salhi, A. Sari, M. Afzaal, F.A. Al-Sulaiman, Effects of carbon-based fillers on thermal properties of fatty acids and their eutectics as phase change materials used for thermal energy storage: a review. J. Energy Storage **35**, 102329 (2021)

11. S.S. Wang, Y.M. Xing, Z.L. Hao, J.B. Yin, X. Hou, Z.X. Wang, Experimental study on the thermal performance of PCMs based heat sink using higher alcohol/graphite foam. Appl. Therm. Eng. **198**, 117452 (2021)

12. Y.P. Yuan, N. Zhang, W.Q. Tao, X.L. Cao, Y.L. He, Fatty acids as phase change materials: a review. Renew. Sustain. Energy Rev. **29**, 482–498 (2014)

13. M.M. Kenisarin, Thermophysical properties of some organic phase change materials for latent heat storage. A review. Solar Energy **107**, 553–575 (2014)

14. M. Li, J.B. Shi, Review on micropore grade inorganic porous medium based form stable composite phase change materials: Preparation, performance improvement and effects on the properties of cement mortar. Constr. Build. Mater. **194**, 287–310 (2019)

15. M.M. Umair, Y. Zhang, K. Iqbal, S.F. Zhang, B.T. Tang, Novel strategies and supporting materials applied to shape-stabilize organic phase change materials for thermal energy storage–A review. Appl. Energy **235**, 846–873 (2019)

16. P.K.S. Rathore, S.K. Shukla, Enhanced thermophysical properties of organic PCM through shape stabilization for thermal energy storage in buildings: a state of the art review. Energy Build. **236**, 110799 (2021)

17. M.Q. Wu, S. Wu, Y.F. Cai, R.Z. Wang, T.X. Li, Form-stable phase change composites: preparation, performance, and applications for thermal energy conversion, storage and management. Energy Storage Mater. **42**, 380–417 (2021)

18. R.A. Rahman, A.H. Lahuri, Ismail, Thermal stress influence on the long-term performance of fast-charging paraffin-based thermal storage. Therm. Sci. Eng. Prog. **37**, 101546 (2022)

19. H.Z. Ke, Q.F. Wei, Using co-electrospinning method to regulate phase change temperatures of fatty acid eutectic/polystyrene/fatty acid eutectic form-stable phase change composite nanofibrous membranes for thermal energy storage. Thermochim. Acta **683**, 178438 (2020)

20. I. Baskar, M. Chellapandian, K. Jeyasubramanian, LA-PA eutectic/nano-SiO_2 composite phase change material for thermal energy storage application in buildings. Constr. Build. Mater. **338**, 127663 (2022)

21. S. Benayache, S. Alleg, A. Mebrek, J.J. Suñol, Thermal and microstructural properties of paraffin/diatomite composite. Vacuum **157**, 136–144 (2018)

22. F.F. Li, H.R. Zhen, L.F. Li, Y.Y. Li, Q.M. Wang, X.M. Cheng, A template-method synthesis of mesoporous-MgO/expanded graphite for enhancing thermal properties of methyl palmitate-lauric acid phase change materials. Mater. Today Energy **26**, 100999 (2022)

23. S.K. Singh, S.K. Verma, R. Kumar, Thermal performance and behavior analysis of SiO_2, Al_2O_3 and MgO based nano-enhanced phase-changing materials, latent heat thermal energy storage system. J. Energy Storage **48**, 103977 (2022)

24. Z.C. Qian, H. Shen, X. Fang, L.W. Fan, N. Zhao, J. Xu, Phase change materials of paraffin in h-BN porous scaffolds with enhanced thermal conductivity and form stability. Energy Build. **158**, 1184–1188 (2018)

25. X.W. Jia, Q.Y. Li, C.H. Ao, R. Hu, T. Xia, Z.H. Xue, Q.H. Wang, X.Y. Deng, W. Zhang, C.H. Lu, High thermal conductive shape-stabilized phase change materials of polyethylene glycol/boron nitride@chitosan composites for thermal energy storage. Compos. A Appl. Sci. Manuf. **129**, 105710 (2020)

26. P. Samiyammal, V. Fuskele, S.K.F. Babavali, N.M. Khan, M.S. Ansari, D.T. Sakhare, Experimental investigations on thermal conductivity and thermal stability of the PCM using Nano-MgO. Mater. Today: Proc. (2022). https://doi.org/10.1016/j.matpr.2022.07.158

27. B.S. Xie, C.C. Li, J. Chen, N. Wang, Exfoliated 2D hexagonal boron nitride nanosheet stabilized stearic acid as composite phase change materials for thermal energy storage. Sol. Energy **204**, 624–634 (2020)

28. X. Fang, L.W. Fan, Q. Ding, X.L. Yao, Y.Y. Wu, J.F. Hou, X. Wang, Z.T. Yu, G.H. Cheng, Y.C. Hu, Thermal energy storage performance of paraffin-based composite phase change materials filled with hexagonal boron nitride nanosheets. Energy Convers. Manage. **80**, 103–109 (2014)

29. Q. He, H. Fei, J.H. Zhou, W.Q. Du, Y.C. Pan, X.M. Liang, Preparation and characteristics of lauric acid-myristic acid-based ternary phase change materials for thermal storage. Mater. Today Commun. **32**, 104058 (2022)

30. C. Li, B. Xie, J. Chen, Graphene-decorated silica stabilized stearic acid as a thermal energy storage material. RSC Adv. **7**, 30142–30151 (2017)

31. B.C. Yang, T. Zhang, J.J. Wang, J. Lv, Y. Zheng, Y. Zhang, Y. Wang, Novel properties of stearic acid/MXen-Graphene oxide shape-stabilized phase change material: ascended phase transition temperature and hierarchical transition. Sol. Energy Mater. Sol. Cells **247**, 111948 (2022)

32. J. Wang, X. Jia, D.G. Atinafu, M. Wang, G. Wang, Y. Lu, Synthesis of "graphene-like" mesoporous carbons for shape stabilized phase change material with high loading capacity and improved latent heat. J. Mater. Chem. A **5**, 24321–24328 (2017)

33. S. Zhang, S. Wang, J. Zhang, Y. Jiang, Q. Ji, Z. Zhang, Z. Wang, Increasing phase change latent heat of stearic acid via nanocapsule interface confinement. J. Phys. Chem. C **117**, 23412–23417 (2013)

34. B. Kersting, M. Salinga, Exploiting nanoscale effects in phase change memories. Faraday Discuss. **213**, 357–370 (2019)

35. C.Q. Zhu, Y.K. Chen, R.S. Cong, F.M. Ran, G.Y. Fang, Improved thermal properties of stearic acid/high density polyethylene/carbon fiber composite heat storage materials. Sol. Energy Mater. Sol. Cells **219**, 110782 (2021)

36. X.B. Gu, P. Liu, L. Bian, H.C. He, Enhanced thermal conductivity of palmitic acid/mullite phase change composite with graphite powder for thermal energy storage. Renew. Energy **138**, 833–841 (2019)

37. A. Sari, Fabrication and thermal characterization of kaolin-based composite phase change materials for latent heat storage in buildings. Energy Build. **96**, 193–200 (2015)

38. Z.S. Zhang, G. Alva, M. Gu, G.Y. Fang, Experimental investigation on n-octadecane/polystyrene/expanded graphite composites as form-stable thermal energy storage materials. Energy **157**, 625–632 (2018)

39. Y.K. Chen, C.L. Xu, R.S. Cong, F.M. Ran, G.Y. Fang, Thermal properties of stearic acid/active aluminum oxide/graphene nanoplates composite phase change materials for heat storage. Mater. Chem. Phys. **269**, 124747 (2021)

40. G.H. Leng, G. Qiao, G.Z. Xu, T. Vidal, Y.L. Ding, Erythritol-Vermiculite form-stable phase change materials for thermal energy storage. Energy Procedia **142**, 3363–3368 (2017)